Journal of the European Ceramic Society 17 (1997) 1513–1521

PII: S0955-2219(97)00038-1
0955-2219/97/$17.00

Preparation and Characterization of $Pr_{1-x}Sr_xMnO_{3\pm\delta}$ ($x=0$, 0·15, 0·3, 0·4, 0·5) as a Potential SOFC Cathode Material Operating at Intermediate Temperatures (500–700°C)

G. Ch. Kostogloudis, N. Vasilakos & Ch. Ftikos

Laboratory of Inorganic Materials Technology, Department of Chemical Engineering, National Technical University of Athens, 9 Heroon Polytechniou Str., Zografou Campus, GR-157 80 Athens, Greece

(Received 18 November 1996; revised version received 13 February 1997; accepted 17 February 1997)

Abstract

The crystal structure, thermal expansion and electrical conductivity of Sr-doped praseodymium manganites ($Pr_{1-x}Sr_xMnO_{3\pm\delta}$ where x = 0, 0·15, 0·3, 0·4, 0·5) were studied in air, and their potential use as cathodes in intermediate temperature SOFCs was evaluated. All compositions have an orthorhombic perovskite-type structure (Pbnm space group). The lattice parameters were determined at room temperature by X-ray powder diffraction. The thermal expansion is almost linear for compositions with $x \geq 0{\cdot}15$. The electrical conductivity can be described by the small polaron hopping conductivity model. The conductivity increases with temperature for all compositions. Both the thermal expansion coefficient (TEC) and the electrical conductivity increase with increasing Sr content, while the activation energy decreases. The low values of the calculated activation energies are in agreement with the small polaron hopping mechanism. Among the compositions studied, $Pr_{0.5}Sr_{0.5}MnO_{3\pm\delta}$, with a TEC value of $12{\cdot}2 \times 10^{-6}\,cm\,(cm\,°C)^{-1}$ and a conductivity value of $226\,S\,cm^{-1}$ at 500°C, seems to be the most promising material that can function as cathode in the intermediate temperature SOFC. © *1997 Elsevier Science Limited.*

1 Introduction

Over the last three decades, there has been a growing interest towards fuel cell development. A fuel cell is an energy conversion device that produces electricity and heat by electrochemical combination of a fuel with an oxidant.[1]

A fuel cell involving a ceramic solid electrolyte and operated at 1000°C was first developed in 1937 by Baur and Preis.[2] Since that time, extensive research programs have been undertaken on solid oxide fuel cells (SOFCs) using solid oxide electrolytes and working between 800 and 1000°C, and great technological progress has been achieved.[1,3]

Since the problem of materials selection for high temperature operation (900–1000°C) has almost been resolved, and the construction and successful operation of SOFC modules has been achieved, the aim of many researchers is for further design optimization and cost reduction. However, operating at these high temperatures has problems associated with the lack of economic balance-of-plant equipment, or reliable interconnection materials (bipolar plates), and there is a requirement to reduce the operating temperature to the intermediate range 700–800°C (for CH_4 fuel) and 450–500°C (for CH_3OH fuel).[4,5] Moreover, operating at intermediate temperatures would greatly reduce material and fabrication problems and improve cell reliability during prolonged operation.[1] Direct methanol SOFCs operating around 500°C may significantly contribute to transport applications as pollution-free power units for electric vehicles.[6]

The high temperature SOFC system usually incorporates yttria stabilized zirconia (YSZ), an oxygen ion conductor, as a solid electrolyte. The conductivity of YSZ is acceptable at high temperatures ($10^{-1}\,S\,cm^{-1}$ at 950°C), but at intermediate temperatures it is substantially reduced ($9 \times 10^{-4}\,S\,cm^{-1}$ at 500°C).[4,5] Other electrolytes, with higher conductivities than YSZ, have been proposed. The most promising ones are those based on ceria (CeO_2) doped with various rare earth oxides.[7,8] Typical conductivity values for

$Ce_{0.9}Gd_{0.1}O_{1.95}$ are 10^{-1} S cm^{-1} at 700°C and 10^{-2} S cm^{-1} at 500°C.[9] The use of such electrolytes in high temperature SOFCs has been excluded for many years because it is known that, when exposed to the reducing atmosphere of the fuel cell anode at elevated temperatures, doped ceria electrolytes become mixed conductors. The electronic charge carriers formed would then short circuit the cell. However, as the temperature is reduced, the ionic domain of the material is increased and doped CeO_2 can be successfully incorporated as electrolyte in SOFCs operating at intermediate temperatures (500–700°C). Moreover, the fact that doped CeO_2 electrolytes have higher thermal expansion coefficients (around $12{\cdot}5\times10^{-6}$ cm (cm °C)$^{-1}$ compared to YSZ (11×10^{-6} cm (cm °C)$^{-1}$), permits the use of electrode materials with higher thermal expansion coefficient values than those already employed. This allows a greater range of oxides to be considered as electrodes.

Operation at intermediate temperatures also requires the selection of an appropriate interconnection material (bi-polar plate). Ceramic materials based on $LaCrO_3$ compositions, which are used for high temperature SOFCs, do not possess sufficient electronic conductivity at intermediate temperatures. Moreover, they are rather expensive due to high fabrication costs. In contrast, it is possible to specify ferritic stainless steel compositions for the bi-polar plate in the temperature range of 500–700°C. A major advantage in using ceria-based electrolytes in conjunction with ferritic stainless steel is their excellent thermal expansion compatibility.[9]

As the selection of materials for the electrolyte and the interconnect is now possible for intermediate temperature SOFCs, attention needs to be focused onto the performance of appropriate electrode materials. The principal objective of our research, therefore, is the preparation and characterization of ceramic materials which can function as cathodes in SOFCs operating at intermediate temperatures (500–700°C). The most promising materials are the mixed (electronic and ionic) conducting perovskite oxides of the structure ABO_3, where A and B are rare earth and transition metals (Mn, Co, Ni, Fe, Cr, Cu), respectively.[10–13] In these oxides it is possible to partially substitute alkaline earth cations (Sr^{2+}, Ca^{2+} or Ba^{2+}) for rare earth cations at the A-site, in order to enhance the conductivity of the cathode material. At present, the materials which draw most attention belong to the systems $La_{1-x}Sr_xMnO_{3\pm\delta}$ and $La_{1-x}(Sr,Ca)_xCo_{1-y}Fe_yO_{3-\delta}$. However, research efforts are still being carried out for rare earth perovskite oxide compositions with improved properties. It has been reported[14] that among various Sr-doped rare earth manganites, those incorporating Pr^{3+} ion at the A-site exhibited the highest electrical conductivity and maintained the lowest overpotential values. However, there is little published information concerning the structural, thermal and electrical properties of doped $PrMnO_3$.

The purpose of this investigation was to evaluate the crystal structure, thermal expansion behavior and electrical conductivity of Sr-doped praseodymium manganites ($Pr_{1-x}Sr_xMnO_{3\pm\delta}$, where $x=0$, 0·15, 0·3, 0·4, 0·5). The effect of Sr content on the properties of these oxides is being discussed.

2 Experimental

The $Pr_{1-x}Sr_xMnO_{3\pm\delta}$ powders were prepared by citrate synthesis and pyrolysis.[15,16] Pr_6O_{11} was dissolved in nitric acid, while $Sr(NO_3)_2$ and $(CH_3COO)_2Mn{\cdot}4H_2O$ were dissolved in distilled water, all in the correct molar proportions. In order to achieve the correct stoichiometric value for each metal in the final product, the exact amount of each metal per g of the respecting reagent was determined by Atomic Absorption Spectroscopy (AAS) before the preparation of the solutions. The individual solutions were mixed together and an aqueous solution of citric acid was added. The amount of citric acid used was that necessary to bind all the metals. The resulting solution is acidic because of the nitric acid used to dissolve the Pr_6O_{11}. It is very important that the pH value remains lower than 7 since, at higher pH values, hydroxides and base salts will appear. The solution was heated over a burner flame until a viscous mass was obtained. A large swelling followed, due to the citric acid, and finally combustion was initiated. After the pyrolysis, a fine homogeneous powder was obtained. The powder was calcined in air at 1100°C for 15 h. The powder was then subjected to a milling process for 72 h (3 days) in a satellite-type milling apparatus. Wet milling with acetone was performed, using zirconia balls. The milled products were dried, and then compacted in cylindrical rods, by isostatic pressing at 300 MPa. The compacts were sintered in air at 1300°C for 15 h. The heating and cooling rate was 1°C min^{-1}. The dimensions of the resulting sintered rods were approximately 6 mm in diameter and 50 mm in length.

The phase analysis and the determination of the lattice parameters at room temperature were carried out by X-ray powder diffraction (XRD) on a SIEMENS diffractometer using CuKα radiation. The diffractometer was operated at 40 kV and 30 mA. XRD spectra were obtained by scanning continuously at a rate of 1·2° 2θ min^{-1} in the range 10–80° 2θ. The unit cell parameters were determined

using the LSUCR (Least squares Unit Cell Refinement) computer program.

The bulk densities of the sintered rods were measured by the Archimedean method using distilled water as the liquid medium. According to this method, the sample is first saturated with water by being in boiling water for 1 h, and then it is weighed three times. The first time the sample is suspended from a wire and weighed while it is immersed in water (mass M_3). The sample is then wiped with a dry cloth only at the surface, so that its pores remain saturated with water, and its mass is measured again (mass M_2). Finally it is dried at 120°C and a last measurement is taken (mass M_1). The density of the sample is calculated using the following equation:

$$d = \frac{M_1 \times d_{H_2O}}{M_2 - M_3 + M_{\text{wire}}} \quad (1)$$

where d_{H_2O} is the density of water and M_{wire} is the mass of the wire, measured while the wire is immersed in the water.

Thermal expansion measurements were carried out on a dilatometer upon cooling from 800 to 100°C in air. The cooling rate was 5°C min^{-1}.

The electrical conductivity was measured by the four-probe DC method on the sintered cylindrical rods. The measurements were performed upon heating from 100 to 800°C in air, and with a heating rate of 5°C min^{-1}. Four platinum (Pt) wire contacts were made, which were painted with silver paint. Two current contacts were made at the rod edges, and two voltage contacts in between at a distance L. The sample was then fired at 500°C for 1 h to allow complete adhesion of the electrodes and reduction of the contact resistance. The sample was placed in a horizontal tube furnace. The voltage (V) between the two inner electrodes and the current intensity (I) were recorded after the sample was left at each temperature at which measurement was taken, for 40 min. The electrical conductivity σ was calculated by the equation:

$$\sigma = \frac{I}{V} \times \frac{L}{A} \quad (2)$$

where A is the cross-sectional area of the rod.

3 Results and Discussion

3.1 Crystal structure

The ideal crystal structure of the perovskite-type oxide ABO_3 has cubic symmetry. The structure consists of corner-shared BO_6 octahedra, while the larger A cation is located at the center of the cubic unit cell. A and B cations and O anion are 12-fold, 6-fold, and 6-fold co-ordinated, respectively.

In the ideal structure the following relation between the ionic radii holds:

$$(r_A + r_O) = \sqrt{2}(r_B + r_O) \quad (3)$$

When A and B are rare earth (RE) and transition metals (Mn, Co, Ni, Fe, Cr, Cu), respectively, the above criterion is not satisfied because of the small size of the RE cation. As a result, the BO_6 octahedra are tilted and rotated to fill the extra space around the RE ion. These rotations cause the unit cell to be smaller and distorted from the ideal cubic cell. As a measure of the deviation from ideality, Goldschmidt[17] introduced a 'tolerance factor' t, defined as:

$$t = (r_A + r_O)/\sqrt{2}(r_B + r_O) \quad (4)$$

If cations RE^{3+} and B^{3+} could be found such that $t = 1$, the ideal cubic perovskite structure would be formed. When t is slightly less than 1, the rhombohedral unit cell is favored. For smaller t, the resulting structure is orthorhombic. For even smaller values of t, non-perovskite structures are formed. It has been reported[18,19] that the lower limit of t for the perovskite structure is around 0·8. Moreover, a boundary has been defined[20] at $t = 0{\cdot}985$, above which rhombohedral structures are formed and below which the atoms form an orthorhombic structure.

In the case of $PrMnO_3$, the value of $t = 0{\cdot}93$ can be obtained from eqn (4) using the following ionic radii, published by Shannon:[21] $r(Pr^{3+}) = 1{\cdot}30$ Å (CN = 12), $r(Mn^{3+}) = 0{\cdot}645$ Å (CN = 6), $r(O^{2-}) = 1{\cdot}40$ Å (CN = 6). By this value of t, the orthorhombic structure can be well-predicted for $PrMnO_3$.

The X-ray powder diffraction patterns of the five oxides of the system $Pr_{1-x}Sr_xMnO_{3\pm\delta}$ ($x = 0$, 0·15, 0·3, 0·4, 0·5) that were prepared are shown in Fig. 1. In all cases, single phase materials were obtained, having the orthorhombic structure, as expected. The patterns were indexed in the same space group (Pbnm) as $GdFeO_3$[22] and the calculated lattice parameters are shown in Table 1. The $GdFeO_3$ structure is probably the most common of all the orthorhombically distorted perovskites. Each cell is built up of four units, and it has the approximate dimensions $\sqrt{2}\alpha_p \times \sqrt{2}\alpha_p \times 2\alpha_p$, where α_p is the lattice parameter of the ideal cubic unit cell. Also, the GdO_{12} polyhedron is severely distorted, showing an (8 + 4) co-ordination.[23]

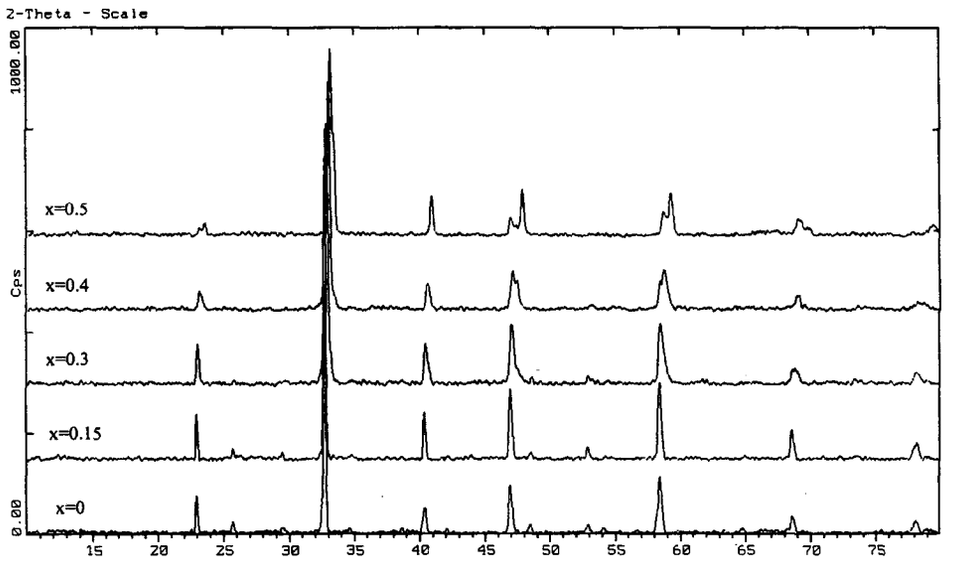

Fig. 1. X-ray powder diffraction patterns of $Pr_{1-x}Sr_xMnO_{3\pm\delta}$.

Table 1. Phase symmetry, lattice parameters, unit cell volume, orthorhombic deformation D(%), and type of orthorhombic structure of the system $Pr_{1-x}Sr_xMnO_{3\pm\delta}$

x (mol)	*Phase symmetry*	*α(Å)*	*b (Å)*	*c (Å)*	*Volume (Å³)*	*c/√2 (Å)*	*α, b, c/√2 relation*	*Orthorhombic deformation D(%)*	*Type of orthorhombic structure*
0	Orthorhombic	5·4674	5·4740	7·7528	232·0	5·4821	$\alpha < b < c/\sqrt{2}$	0·092	O-type
0·15	Orthorhombic	5·4721	5·4711	7·7431	231·8	5·4752	$\alpha \approx b < c/\sqrt{2}$	0·029	O-type
0·3	Orthorhombic	5·4598	5·4681	7·7416	231·1	5·4741	$\alpha < b < c/\sqrt{2}$	0·092	O-type
0·4	Orthorhombic	5·4473	5·4607	7·6689	228·1	5·4227	$c/\sqrt{2} < \alpha < b$	0·255	O′-type
0·5	Orthorhombic	5·4309	5·5165	7·5937	227·5	5·3696	$c/\sqrt{2} < \alpha < b$	0·948	O′-type

It can be seen from Fig. 1 that the characteristic splitting of the X-ray peaks in the case of $x=0{\cdot}4$ and $x=0{\cdot}5$ is indicative of the orthorhombic distortion in these structures. The other compounds are less distorted, and the splitting of the diffraction peaks does not occur. The presence of additional peaks, though, (at $2\theta=25{\cdot}7°$ and $48{\cdot}5°$, for example) in the samples with $x=0$, 0·15 and 0·3 demonstrate the orthorhombic distortion of their unit cells.

Two types of orthorhombic structures are distinguished. The O-type structure, which is characterized by the relationship $\alpha \leq c/\sqrt{2} \leq b$, exists when the lattice deformation is relatively small, while the O′-type structure, with $c\sqrt{2} \leq \alpha \leq b$, exists in the case of enhanced lattice deformation. The values of α, b and $c/\sqrt{2}$ for $Pr_{1-x}Sr_xMnO_{3\pm\delta}$, as well as the relation among them, are shown in Table 1. The evolution of these parameters as x increases from $x=0$ to 0·5 is illustrated in Fig. 2. It can be seen that the structure is O-type for low values of x ($x=0$, 0·15 and 0·3), and it becomes O′-type at higher x values ($x=0{\cdot}4$, 0·5).

From Fig. 2, it is evident that the deviation among the parameters α, b and $c/\sqrt{2}$ is small when $x=0$–0·3, while it is increased when $x=0{\cdot}4$ and 0·5. This observation is in accordance with the evolution of the splitting of the diffraction peaks noticed in the XRD patterns in Fig. 1, and indicates that the orthorhombic lattice deformation is enhanced as x is increased in the range $x=0$–0·5. In order to quantitatively express the deviation of the unit cell from the orthorhombic structure, the quantity D (% orthorhombic deformation) is defined:

$$D = \frac{1}{3}\sum_{i=1}^{3} \left|\frac{\alpha_i - \bar{\alpha}}{\bar{\alpha}}\right| \cdot 100 \qquad (5)$$

where $\alpha_1 = \alpha$, $\alpha_2 = b$, $\alpha_3 = c/\sqrt{2}$, and $\bar{\alpha} = (\alpha bc/\sqrt{2})^{1/3}$. The value of D was calculated for each compound (Table 1 and Fig. 2). It can be seen that for $x=0$–0·3, D is very small, while for higher values of x, D increases considerably. Sample $x=0{\cdot}5$, in particular, shows the largest deformation, as expected considering its XRD pattern.

To illustrate the effect of Sr substitution on the lattice parameters, the pseudo-cubic lattice constant (α') is defined as the cube root of the unit cell volume per ABO_3 unit:

$$\alpha' = (V/4)^{1/3} \qquad (6)$$

As shown in Fig. 3, α' decreases with increasing Sr content. This can be explained considering the defect structure of $Pr_{1-x}Sr_xMnO_{3\pm\delta}$.

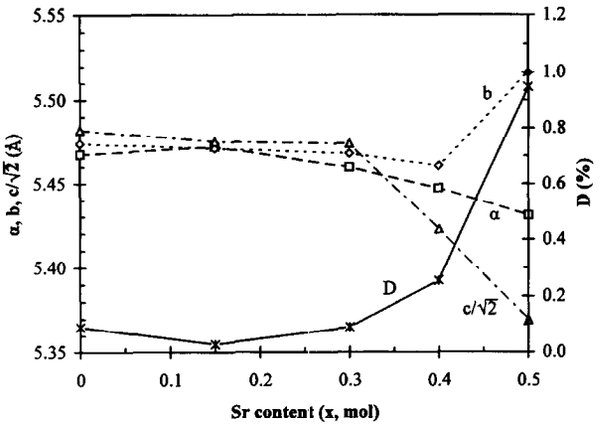

Fig. 2. The lattice parameters ($\alpha, b, c/\sqrt{2}$) and the orthorhombic deformation (D, %) of $Pr_{1-x}Sr_xMnO_{3\pm\delta}$ as a function of Sr content (x, mol).

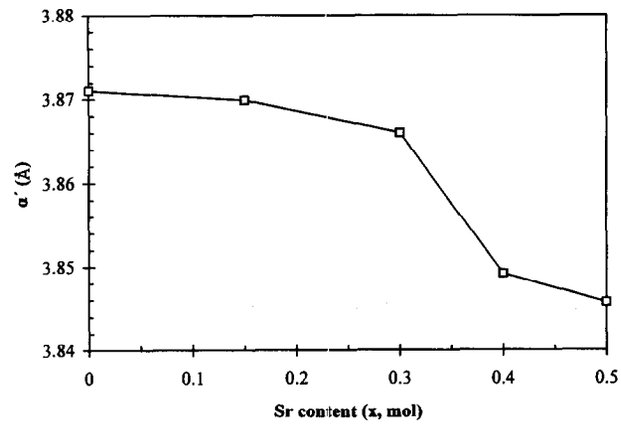

Fig. 3. Pseudo-cubic lattice constant (α') as a function of Sr content (x, mol).

In the discussion that follows, a simplified defect model has been adopted[24] which is valid for all rare earth manganites. In this model, it is assumed that the valence of the RE cation is 3+ but, in the case of praseodymium ion which has two possible valence states (3+ and 4+), there might be a problem concerning the applicability of the model. However, it has been reported[25] that all the praseodymium ions in praseodymium manganites are present in the trivalent state. Moreover, Lacorre *et al.*[20] used bond–valence theory in order to measure the charge on the Pr site in $PrNiO_3$, and they found a value of +3·12, which is very close to the ideal value +3·0. They concluded, concerning the uncertainty of the calculation, that the Pr ion in $PrNiO_3$ is primarily Pr^{3+} with little (< 10%), if any, Pr^{4+} present. We, therefore, assume that Pr^{3+} is the only praseodymium ion present in the perovskite lattice.

At high oxygen partial pressures, oxygen nonstoichiometry δ in rare earth manganites has positive values.[26–30] The oxygen excess may result from an equal amount of A and B site vacancies by a defect reaction[31] which, in the case of $PrMnO_{3\pm\delta}$, can be written as:

$$6Mn_{Mn}^{x} + \frac{3}{2}O_2 \Longleftrightarrow V_{Pr}''' + V_{Mn}''' + 6Mn_{Mn}^{\cdot} + 3O_o^x \quad (7)$$

where, in Kröger-Vink notation,[32] Mn_{Mn}^{x} is a Mn^{3+} cation on a regular site, V_{Pr}''' and V_{Mn}''' are a Pr^{3+} and a Mn^{3+} vacancy, respectively, $Mn_{Mn}^{\cdot}$ is a Mn^{4+} cation on a Mn^{3+} lattice position and O_o^x is an O^{2-} ion on a regular site in the perovskite lattice. The substitution of Sr^{2+} for Pr^{3+} is electronically compensated by the formation of Mn^{4+} ($Mn_{Mn}^{\cdot}$) cations:

$$SrMnO_3 \xrightarrow[PrMnO_3]{} Sr_{Pr}' + Mn_{Mn}^{\cdot} + 3O_o^x \quad (8)$$

At relatively low oxygen pressure, oxygen vacancies ($V_o^{\cdot\cdot}$) are formed and Mn^{4+} cations are reduced to Mn^{3+}:

$$2Mn_{Mn}^{\cdot} + O_o^x \Longleftrightarrow 2Mn_{Mn}^{x} + V_o^{\cdot\cdot} + \frac{1}{2}O_2 \quad (9)$$

At room temperature, in air ($pO_2 = 0{\cdot}21$ atm), the oxides $Pr_{1-x}Sr_xMnO_{3\pm\delta}$ show a slight excess of oxygen,[30,33] which means that the defect reactions (7) and (8) are favored. As x increases, more Sr^{2+} ions are substituted for Pr^{3+} ions, causing a charge imbalance. In order to maintain electrical neutrality, Mn^{3+} ions are oxidized to form the smaller Mn^{4+} ions according to eqn (8), which has, as a result, the net decrease in the average radius of the Mn ions. In addition, according to Pauling's second rule (concerning bond strength),[34] the tetravalent Mn ions will strengthen the Mn–O bonds in the MnO_6 octahedra. As a result, both the size of MnO_6 octahedra and the volume of the perovskite unit cell decrease with increasing Sr content.

3.2 Density

In order to measure the thermal expansion coefficient and electrical conductivity of the ceramic materials, dense samples must be obtained. Densities of >90% of the theoretical value are considered satisfactory.

Theoretical density (or X-ray density) can be calculated (in $g\,cm^{-3}$) by the equation:[35]

$$d_{th} = z\frac{M}{V \times 0 \cdot 6023} \quad (10)$$

where M (in atomic-weight units) is the mass of the atomic ensemble constituting one unit of the chemical formula, z is the number of such chemical units in one unit cell of the crystal, and V (in $Å^3$) is the volume of the crystalline unit cell as determined by X-ray diffraction ($V = abc$ for the orthorhombic

Table 2. Sintering temperature, measured sintered density (d), theoretical XDR density (d_{th}), and d/d_{th} (%) of $Pr_{1-x}Sr_xMnO_{3\pm\delta}$

x (mol)	*Sintering temperature (°C)*	*Sintered density d (g cm^{-3})*	*XRD density d_{th} (g cm^{-3})*	*d/d_{th} (%)*
0	1300	6·49	6·98	93·0
0·15	1300	6·39	6·76	94·5
0·3	1300	6·37	6·55	97·3
0·4	1300	6·20	6·48	95·7
0·5	1300	5·99	6·34	94·5

unit cell). For an orthorhombic unit cell of the $GdFeO_3$-type structure, $z=4$, as mentioned in the previous section. M was calculated assuming the stoichiometric perovskite $Pr_{1-x}Sr_xMnO_3$, since the oxygen non-stoichiometry was not determined. The departure from stoichiometry is not expected to be considerable, though,[33] and so the error in the calculation of d_{th} is very small.

The sintering temperature, the measured sintered density (d), the theoretical XRD density (d_{th}), and the d/d_{th} (%) are given in Table 2. All samples have densities well above 90% of the theoretical values.

3.3 Thermal expansion

Linear thermal expansion curves for $Pr_{1-x}Sr_xMnO_{3\pm\delta}$ (x = 0, 0·15, 0·3, 0·4, 0·5), obtained upon cooling from 800 to 100°C in air, are shown in Fig. 4. The hysteresis during the heating and cooling cycle was negligible. For $x=0$, the thermal expansion curve shows almost no increase in the temperature range 350–550°C. Before and after this region the increase is linear. Moreover, the slope of the curve in the region above 550°C is greater than that in the region below 350°C. The break in the thermal expansion curve may be attributed to a structure transition, as will be confirmed in the next section by electrical conductivity measurements. For the compositions with $x\geq 0{\cdot}15$, an almost linear length increase is noticed. At high temperatures, however, the curves become steeper. This may be attributed to the loss of lattice oxygen at high temperatures, and the formation of oxygen vacancies [eqn (9)]. For every $V_O^{\cdot\cdot}$ which is formed,

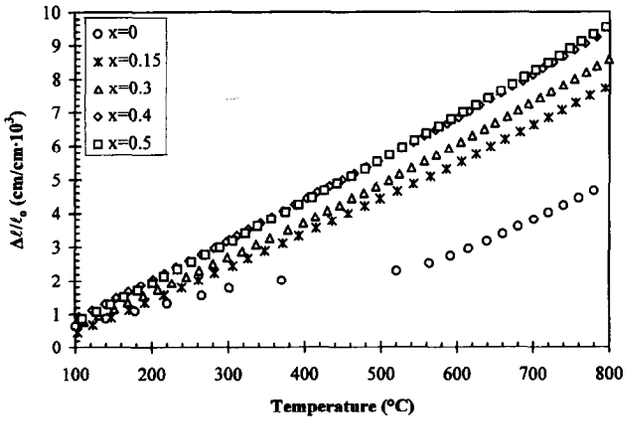

Fig. 4. Linear thermal expansion curves for $Pr_{1-x}Sr_xMnO_{3\pm\delta}$ in air.

two manganese ions are reduced from higher to lower valence state ($Mn^{4+}\rightarrow Mn^{3+}$). Considering the larger size of the Mn^{3+} cation with respect to Mn^{4+}, it is apparent that an increase in the unit cell volume is to be expected as the number of oxygen vacancies is increased. In addition, the reduction of the manganese cations causes a decrease in the Mn–O bond strength according to Pauling's second rule,[34] and hence the size of MnO_6 octahedra increases.

Linear thermal expansion coefficients (TEC) calculated from the thermal expansion curves by simple linear regression at given temperature ranges are listed in Table 3. In Fig. 5, the linear TEC values corresponding to the temperature range from room temperature up to 500°C, as well as at 700°C, are plotted as a function of x. It is obvious that the thermal expansion coefficient of $Pr_{1-x}Sr_xMnO_{3\pm\delta}$ increases as the degree of Sr-doping is increased, at both temperature regions. The best thermal expansion compatibility with the doped-CeO_2 electrolytes at the temperature range up to 500°C (the operating temperature of the direct methanol SOFC) is obtained when $x=0{\cdot}5$. Namely, the linear TEC of $Pr_{0{\cdot}5}Sr_{0{\cdot}5}MnO_{3\pm\delta}$ is $12{\cdot}2\times10^{-6}$ cm (cm °C)$^{-1}$, which is almost equal to that of doped-CeO_2 electrolytes (around $12{\cdot}5\times10^{-6}$ cm (cm °C)$^{-1}$. At 700°C (the operating temperature of the cell when CH_4 fuel is to be used) the TEC of $Pr_{0{\cdot}5}Sr_{0{\cdot}5}MnO_{3\pm\delta}$ cathode material increases and has a value of $13{\cdot}6\times10^{-6}$ cm (cm°C)$^{-1}$, which is about 9% greater than that of the doped-CeO_2 electrolyte. This magnitude of thermal expansion mismatch is acceptable, however, and would not constitute a problem for the successful operation of the cell.

3.4 Electrical conductivity

The logarithm of electrical conductivity (logσ) of $Pr_{1-x}Sr_xMnO_{3\pm\delta}$ measured upon heating from 100 to 800°C in air, is plotted as a function of temperature in Fig. 6. It can be seen that σ increases with temperature for all compositions ($x=0$–$0{\cdot}5$). At 500°C, the electrical conductivities are 23, 78, 183, 214 and 226 S cm^{-1} for $x=0$, 0·15, 0·3, 0·4 and 0·5, respectively.

For $x=0$, a break on the electrical conductivity curve of Fig. 6 is noticed in the temperature range

400–550°C. A break was also observed in the thermal expansion curve of the material at the same temperature range, as was shown in the previous section. This behavior suggests that a structure transition occurs at 400–550°C for $PrMnO_{3\pm\delta}$.

For the system $Pr_{1-x}Sr_xMnO_{3\pm\delta}$, the temperature dependence of conductivity shown in Fig. 6 can be described by the small polaron hopping conductivity model.[36] The band model is not appropriate in this case, since the charge carriers (electrons or holes) are localized and they are regarded as hopping from site to site. Hopping conduction occurs when ions of the same type but with oxidation states differing by unity occur on equivalent lattice sites and is, therefore, likely to be observed in transition metal oxides. In the case of $Pr_{1-x}Sr_xMnO_{3\pm\delta}$, Mn^{4+} cations ($Mn^{\cdot}_{Mn}$ using Kröger-Vink notation) are formed according to eqns (7) and (8). The system $Mn^{3+}-Mn^{4+}$ can be regarded as a two-Mn^{3+} system with an additional hole (p-type conductivity). The energy of the hole is given by:[28]

$$E = \frac{kQ^2}{2} \pm \sqrt{\ell^2 Q^2 + \beta^2} \qquad (11)$$

where k = force constant, ℓ = parameter related to the bond length, β = overlap integral and Q describes the vibrational motion. In eqn (11), ℓ^2/k favors the localization and β favors the delocalization. If $\beta \approx \ell^2/k$ the hole is localized but with the possibility to hop between sites. Hopping conduction depends on the concentration of Mn^{4+}, as well as on their mobility.

Figure 7 shows the logσ of the system $Pr_{1-x}Sr_xMnO_{3\pm\delta}$, as a function of x, for the intermediate temperatures 500, 600 and 700°C. The conductivity increases with Sr content in all cases. This can be explained considering eqn (8). It can be seen that the charge difference between Pr^{3+} and Sr^{2+} ions is compensated by the formation of Mn^{4+} ions. As the Sr content is increased, the concentration of Mn^{4+} is increased and, therefore, the conductivity increases. With increasing temperature, the conductivity of $Pr_{1-x}Sr_xMnO_{3\pm\delta}$ increases for $x = 0$–0·5 (Figs 6 and 7). Temperature affects both the mobility and the concentration of Mn^{4+} ions. The carrier (Mn^{4+}) mobility is temperature activated, while the Mn^{4+} concentration is reduced at elevated temperatures due to the formation of oxygen vacancies [eqn (9)]. However, the extent at

Table 3. Linear thermal expansion coefficients (TEC) of $Pr_{1-x}Sr_xMnO_{3\pm\delta}$, calculated from the thermal expansion curves of Fig. 4

x (mol)	*Temperature range (°C)*	*Linear TEC [cm (cm°C)$^{-1}$×10^6]*
0	100–350	5·5
	550–800	10·3
0·15	100–600	10·0
	600–800	11·7
0·3	100–500	10·5
	500–800	12·5
0·4	100–600	11·9
	600–800	13·3
0·5	100–600	12·2
	600–800	13·6

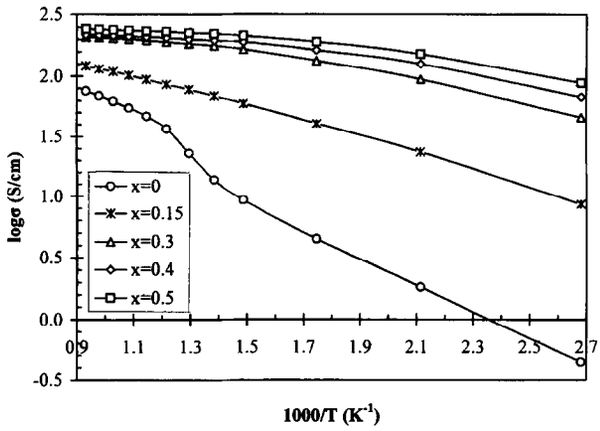

Fig. 6. Logσ versus 1000/T for $Pr_{1-x}Sr_xMnO_{3\pm\delta}$ in air.

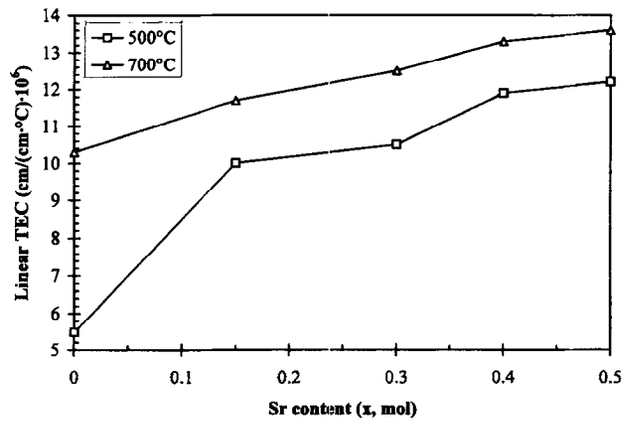

Fig. 5. Linear thermal expansion coefficient (TEC) values of $Pr_{1-x}Sr_xMnO_{3\pm\delta}$ at 500°C and 700°C as a function of Sr content (x, mol) in air.

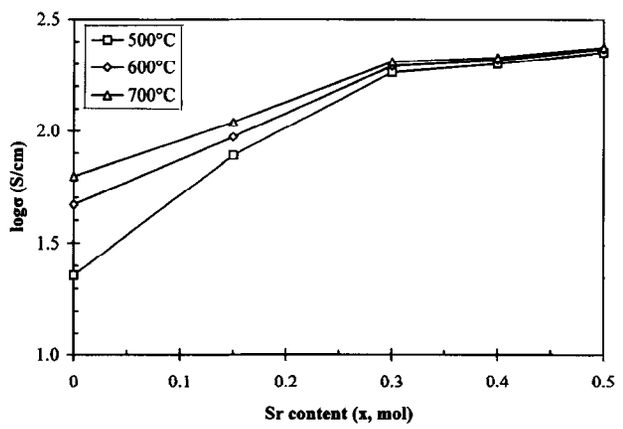

Fig. 7. Log electrical conductivity of $Pr_{1-x}Sr_xMnO_{3\pm\delta}$ as a function of Sr content (x, mol) in air, at temperatures 500, 600 and 700°C.

which oxygen vacancies are formed is limited in the case of rare earth manganites,[37] and the effect of the increase of carrier mobility prevails, giving rise to the conductivity increase.

The temperature dependence of electrical conductivity through the small polaron hopping mechanism is generally expressed as

$$\sigma = \frac{A}{T^s}\exp(-E_a/kT) \qquad (12)$$

in which E_a is the activation energy for hopping conduction, k is the Boltzmann constant, T is the absolute temperature and A is the pre-exponential factor that contains a number of constants like the number of charge carriers and the average distance between the Mn ions. The exponent s is equal either to 1 or to 3/2 for an adiabatic or a non-adiabatic hopping process respectively. The plot of $\log\sigma T^s$ versus 1/T should give a straight line. For $Pr_{1-x}Sr_xMnO_{3\pm\delta}$, a somewhat better linear fit was obtained for $s=3/2$, suggesting a non-adiabatic hopping process. The activation energies are calculated using simple linear regression, from the slopes of the linear parts of the $\log\sigma T^{3/2}$ versus $1000\,T^{-1}$ plots (Fig. 8). Table 4 lists the E_a values obtained over the indicated temperature ranges. The calculated activation energies range from 14·2 kJ mol^{-1} (0·147 eV) to 5·3 kJ mol^{-1} (0·055 eV) and they are comparable with those observed for

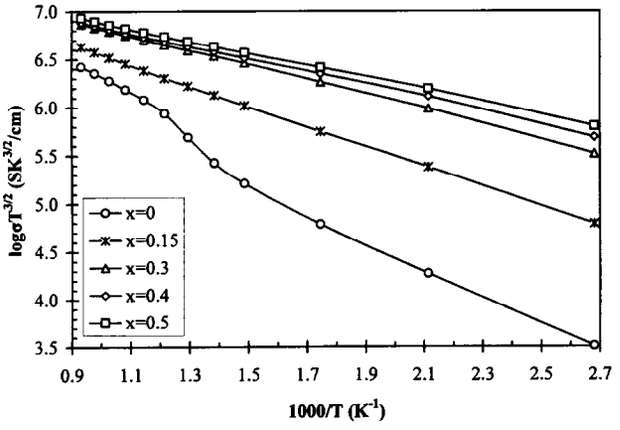

Fig. 8. $\log\sigma T^{3/2}$ versus 1000/T for $Pr_{1-x}Sr_xMnO_{3\pm\delta}$ in air.

Table 4. Activation energies for the electrical conductivity of $Pr_{1-x}Sr_xMnO_{3\pm\delta}$ through the small polaron hopping mechanism, calculated from the curves of Fig. 8

x (mol)	*Temperature range (°C)*	E_a	
		kJ/mol	*eV*
0	100–400	11·76	0·122
	550–800	14·22	0·147
0·15	100–800	8·71	0·090
0·3	100–800	6·34	0·066
0·4	100–800	5·58	0·058
0·5	100–800	5·26	0·055

other rare earth manganites.[28,38,39] The low activation energies are in agreement with the suggestion of the small polaron hopping conduction mechanism described above for $Pr_{1-x}Sr_xMnO_{3\pm\delta}$. The higher E_a value for the undoped compound could be due to the relatively low carrier concentration. The two values of E_a obtained for this compound may be attributed to the structural transition.

The incorporation of Sr in $Pr_{1-x}Sr_xMnO_{3\pm\delta}$ leads to a decrease of the activation energy as shown in Table 4. As Sr content increases, the concentration of Mn^{4+} is increased. The smaller radius of Mn^{4+} with respect to Mn^{3+} reduces the Mn–O distance and brings the Mn–O–Mn angle closer to 180°. As a consequence, the overlap integral β in eqn (11) increases, and the activation energy E_a becomes smaller.[28]

4 Conclusions

The oxides in the system $Pr_{1-x}Sr_xMnO_{3\pm\delta}$ with $x=0$, 0·15, 0·3, 0·4, 0·5 were all found to be single phase. They have a perovskite-type structure with orthorhombic symmetry (Pbnm space group). The orthorhombic deformation is increased for higher values of x. The unit cell volume decreases with increasing Sr content due to the formation of Mn^{4+} cations which are much smaller than Mn^{3+} cations.

The thermal expansion is almost linear for compositions with $x \geq 0{\cdot}15$. At high temperatures, the curves become steeper, probably due to the loss of lattice oxygen and the formation of oxygen vacancies. A structure transition occurs at intermediate temperatures on the undoped sample, confirmed by both the thermal expansion behavior and the electrical conductivity measurement. The TEC values increase as the degree of Sr-doping is increased.

The electrical conductivity of $Pr_{1-x}Sr_xMnO_{3\pm\delta}$ is p-type and can be described by the small polaron hopping mechanism. The Sr addition is primarily compensated by the formation of Mn^{4+} cations. With increasing Sr content, the conductivity is increased, due to the increase in the concentration of Mn^{4+} cations. The conductivity increases with temperature for all compositions ($x=0$–0·5). This is because the mobility of the charge carriers (Mn^{4+}) is temperature activated. The temperature dependence of electrical conductivity through the small polaron hopping mechanism suggests a non-adiabatic hopping process. The calculated activation energies decrease with increasing Sr content. The low values of the activation energies are in agreement with the small polaron hopping mechanism.

Among the examined oxides of the system $Pr_{1-x}Sr_xMnO_{3\pm\delta}$ ($x=0$, 0·15, 0·3, 0·4, 0·5) the

composition with $x=0{\cdot}5$ shows the best properties required for an intermediate temperature SOFC cathode, for the following reasons:

(a) no phase transition is observed within the investigated temperature range. This is confirmed by both thermal expansion and electrical conductivity measurements;
(b) it shows excellent thermal expansion compatibility with the doped-CeO_2 solid electrolyte at the operating temperature range of the direct methanol SOFC (from room temperature up to 500°C). Namely, the linear TEC value of $Pr_{0{\cdot}5}Sr_{0{\cdot}5}MnO_{3\pm\delta}$ is $12{\cdot}2\times10^{-6}$ cm (cm °C)$^{-1}$, which is almost equal to that of the doped-CeO_2 electrolytes (around $12{\cdot}5\times10^{-6}$ cm (cm °C)$^{-1}$);
(c) its electrical conductivity value of 226 S cm^{-1} at 500°C is satisfactory for SOFC operation (consider that $La_{0{\cdot}84}Sr_{0{\cdot}16}MnO_{3\pm\delta}$, which is a well established high temperature SOFC cathode material, has a conductivity value of 190 S cm^{-1} at 1000°C).

Therefore, $Pr_{0{\cdot}5}Sr_{0{\cdot}5}MnO_{3\pm\delta}$ is a promising cathode material for the intermediate temperature SOFC. However, further investigation is needed concerning its chemical compatibility with other cell components, its oxygen ion conductivity and its catalytic activity for oxygen reduction before it is considered acceptable for use as cathode in an SOFC.

Acknowledgement

The authors wish to thank Professor B. C. H. Steele of the Department for Materials, Imperial College, London for very helpful and friendly discussions and collaboration.

References

1. Minh, N. Q., *Journal of Am. Ceram. Soc.*, 1993, **76**, 563.
2. Baur, E. and Preis, H., *Z. Elektrochem.*, 1937, **43**, 727.
3. Hammou, A., In *Advances in Electrochemical Science and Engineering*, Vol. 2, ed. H. Gerischer and C. W. Tobias. VCH, 1992, p. 87.
4. Steele, B. C. H., In *Proceedings of the 14th Risø International Symposium on Materials Science: High Temperature Electrochemical Behaviour of Fast Ion and Mixed Conductors*, eds F. W. Poulsen, J. J. Bentzen, T. Jacobsen, E. Skou and M. J. L. Østergård. Risø National Laboratory, Roskilde, Denmark, 1993, p. 423.
5. Steele, B. C. H., *Solid State Ionics*, 1995, **75**, 157.
6. Steele, B. C. H., *Mater. and Design*, 1990, **11**, 4.
7. Eguchi, K., Setoguchi, T., Inoue, T. and Arai, H., *Solid State Ionics*, 1992, **52**, 165.
8. Inaba, H. and Tagawa, H., *Solid State Ionics*, 1996, **83**, 1.
9. Steele, B. C. H., *Phil. Trans. R. Soc. Lond. A*, 1996, **354**, 1695.
10. Tedmon, C. S., Spacil, H. S. and Mittof, S. P., *Journal of Electrochem. Soc.*, 1969, **116**, 1170.
11. Ohno, Y., Nagata, S. and Sato, H., *Solid State Ionics*, 1981, **3/4**, 439.
12. Isaacs, H. S. and Olmer, L. J., *Journal of Electrochem. Soc.*, 1982, **129**, 436.
13. Priestnall, M. A. and Steele, B. C. H., In *Proceedings of the First International Symposium on Solid Oxide Fuel Cells*, Vol. 89-11, ed. S. C. Singhal. The Electrochemical Society, Inc., Pennington, New Jersey, 1989, p. 157.
14. Ishihara, T., Kudo, T., Matsuda, H. and Takita, Y., *Journal of Electrochem. Soc.*, 1995, **142**, 1519.
15. Baythoun, M. S. G. and Sale, F. R., *Journal of Mater. Sci.*, 1982, **17**, 2757.
16. Blank, D.H.A., Kruidhof, H. and Flokstra, J., *Journal of Phys. D*, 1988, **21**, 226.
17. Goldschmidt, V. M., Skrifter Norske Videnskaps-Akad. Oslo. I. Mathemat. Naturwiss. Klasse N°8, 1926.
18. Megaw, H. D., *Trans. Faraday Soc. A*, 1946, **42**, 224.
19. Ohbayashi, H., Kudo, T. and Gejo, T., *Jpn. Journal of Appl. Phys.*, 1974, **13**, 1.
20. Lacorre, P., Torrance, J. B., Pannetier, J., Nazzal, A. I., Wang, P. W. and Huang, T. C., *Journal of Solid State Chem.*, 1991, **91**, 225.
21. Shannon, R. D., *Acta Crystallogr.*, 1976, **A32**, 751.
22. Geller, S., *Journal of Chem. Phys.*, 1956, **24**, 1236.
23. Baran, E. J., *Catal. Today*, 1990, **8**, 133.
24. Anderson, H. U., *Solid State Ionics*, 1992, **52**, 33.
25. Pollert, E., Krupicka, S. and Kuzmicova, E., *Journal of Phys. Chem. Solids*, 1982, **43**, 1137.
26. Tofield, B. C. and Scott W. C., *Journal of Solid State Chem.*, 1974, **10**, 183.
27. Takeda, Y., *Mater. Res. Bull.*, 1991, **26**, 153.
28. van Roosmalen, J. A. M., Huijsmans, J. P. P. and Plomp, L., *Solid State Ionics*, 1993, **66**, 279.
29. Kamegashira, N. and Miyazaki, Y., *Mater. Res. Bull.*, 1984, **19**, 1201.
30. Cherepanov, V. A., Burkhatova, L. Yu., Petrov, A. N. and Voronin, V. I., *Journal of Solid State Chem.*, 1995, **118**, 53.
31. Kuo, J. H., Anderson, H. U. and Sparlin, D. M., *Journal of Solid State Chem.*, 1989, **83**, 52.
32. Kröger, F. A. and Vink V. J., In *Solid State Physics*, Vol. 3, ed. F. Seitz and D. Turnbull. Academic Press, New York, 1956, p. 307.
33. Knízek, K., Jirak, Z., Pollert, E. and Zounova, F., *Journal of Solid State Chem.*, 1992, **100**, 292.
34. Pauling, L., *The Nature of the Chemical Bond*, 3rd. edn. Cornell University Press, Ithaca, N.Y., 1960.
35. Raman, S. and Katz, J. L., In *Handbook of X-Rays*, ed. E. F. Kaelble. McGraw-Hill, New York, 1967, pp. 29.1–29.2.
36. Cox, P. A., *The Electronic Structure and Chemistry of Solids*. Oxford University Press, Oxford, 1987.
37. Zhang, H. M., Yamazoe, N. and Teraoka, Y., *Journal of Mater. Sci. Lett.*, 1989, **8**, 995.
38. Shuk, P., Tichonova, L. and Guth, U., *Solid State Ionics*, 1994, **68**, 177.
39. Mackor, A., Koster, T. P. M., Kraaijkamp, J. G., Gerretsen, J. and van Eijk, J. P. G. M., In *Proceedings of the Second International Symposium on Solid Oxide Fuel Cells*, ed. F. Grosz, P. Zegers, S. C. Singhal and O. Yamamoto. Commission of the European Communities, Brussels, 1991.